ACS APPLIED MATERIALS & INTERFACES

Research Article

www.acsami.org

# Vapor Synthesis and Thermal Modification of Supportless Platinum–Ruthenium Nanotubes and Application as Methanol Electrooxidation Catalysts

Robert W. Atkinson, III,[†] Raymond R. Unocic,[‡] Kinga A. Unocic,[§] Gabriel M. Veith,[§] Thomas A. Zawodzinski, Jr.,[†,§] and Alexander B. Papandrew*,[†]

[†]Department of Chemical and Biomolecular Engineering, University of Tennessee, Knoxville, Tennessee 37996, United States

[‡]Center for Nanophase Materials Sciences and [§]Materials Science and Technology Division, Oak Ridge National Laboratory, Oak Ridge, Tennessee 37831, United States

Supporting Information

**ABSTRACT:** Metallic, mixed-phase, and alloyed bimetallic Pt–Ru nanotubes were synthesized by a novel route based on the sublimation of metal acetylacetonate precursors and their subsequent vapor deposition within anodic alumina templates. Nanotube architectures were tuned by thermal annealing treatments. As-synthesized nanotubes are composed of nanoparticulate, metallic platinum and hydrous ruthenium oxide whose respective thicknesses depend on the sample chemical composition. The Pt-decorated, hydrous Ru oxide nanotubes may be thermally annealed to promote a series of chemical and physical changes to the nanotube structures, including alloy formation, crystallite growth, and morphological evolution. Annealed Pt–Ru alloy nanotubes and their as-synthesized analogs demonstrate relatively high specific activities for the oxidation of methanol. As-synthesized, mixed-phase Pt–Ru nanotubes (0.39 mA/cm$^2$) and metallic alloyed $Pt_{64}Ru_{36}$NTs (0.33 mA/cm$^2$) have considerably higher area-normalized activities than PtRu black (0.22 mA/cm$^2$) at 0.65 V vs RHE.

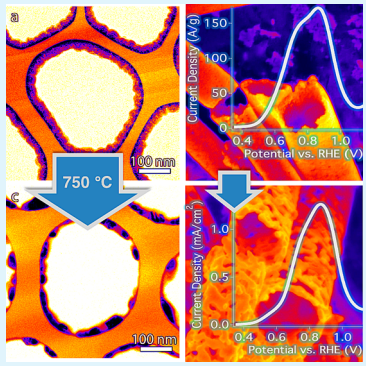


**KEYWORDS:** *chemical vapor deposition, electrocatalysts, nanotubes, anodic alumina, template, extended surface catalysts, alloy, fuel cell*

## 1. INTRODUCTION

Unsupported, high aspect ratio, nanostructured catalysts, or extended surface catalysts, remain promising candidates as oxygen reduction and alcohol oxidation catalysts for fuel cells. These extended surface catalysts usually demonstrate higher specific activities[1,2] compared to their zero-dimensional nanoparticle counterparts due to unique anisotropic, electronic, surface, and structural properties.[3,4] One-dimensional nanostructures are less susceptible to the common degradation modes of conventional carbon-supported nanoparticle catalysts in an operational fuel cell, such as carbon-support corrosion and nanoparticle dissolution, aggregation, and Ostwald ripening.[5−7] These anisotropic catalysts typically feature lower crystal defect populations, minimizing the surface energies of the structures.[8−10] As a result, extended surface catalysts are less vulnerable than small nanoparticles to dissolution and ripening.[8,9,11,12] High aspect ratio extended catalysts could circumvent the need for a carbon support, and subsequently, devices based on this motif would not be constrained by problems related to carbon corrosion or oxidation.[5,13,14]

Numerous synthetic strategies, a complete review of which would exceed the scope of this introduction, have been reported for the production of high-quality, anisotropic, metallic nanostructures. Each technique bears its own strengths and limitations.[8,9] Galvanic displacement has been used to synthesize noble-metal-decorated or completely displaced metal templates of arbitrary shape by the replacement of the template metal with a more-noble metal.[15,16] The nobility of the selected metals restricts the sequencing of layered materials, and residual amounts of common template metals are susceptible to dissolution, migration, and adverse plating during fuel cell operation.[14] Atomic layer deposition (ALD) allows for the precise control of film thickness with the ability to produce alternating layers of atomically precise films but in some cases requires postprocessing to remove undesired impurities,[17] and like chemical vapor deposition, the equipment required is prohibitively expensive. Physical vapor deposition (PVD) has also been used for thin film deposition, but line-of-sight issues limit the technique for conformal film deposition on substrates with high aspect ratio shapes. Though colloidal and other solution-based methods do not require an expensive apparatus for synthesis, surfactants that may be used for shape control can adsorb strongly to the catalyst surface, blocking active sites for the intended reaction and requiring additional processing steps prior to use.[9,18−20]

Received: November 24, 2014
Accepted: April 23, 2015
Published: April 23, 2015





DOI: 10.1021/am508228b
ACS Appl. Mater. Interfaces 2015, 7, 10115−10124

In light of the limitations of some other techniques used to synthesize extended nanostructures, we have established an alternative process for developing monometallic, discretely layered bimetallic, and alloyed bimetallic nanotubes based on a modified chemical vapor deposition (CVD) method that does not require the expensive instrumentation required for conventional CVD.[21−23] Metalorganic precursors are decomposed by heat treatment in a vacuum oven below 250 °C to deposit conformal nanoparticle films along the channels of a porous anodic alumina (AAO) membrane. Unlike galvanic displacement, metals may be deposited in any order, and the initial deposition of a metal has been observed to seed the subsequent vapor deposition of the second metal within the template. Following metal impregnation, the thermally stable AAO templates may be annealed in various gas environments to induce phase transitions, morphological evolution, alloy formation, and grain growth. The ability to control grain growth by adjusting the temperature of the heat treatment is a valuable asset of this postsynthesis annealing technique considering the influence of particle size on activity, which is well-known in the case of oxygen reduction in acidic media[24,25] and recently shown to have an impact on hydrogen oxidation in alkaline conditions.[26] Following thermal treatment, the nanotubes may be recovered by dissolution of the sacrificial template. Our group has previously vapor deposited porous platinum nanotubes using this technique, which demonstrated very high specific activity, comparable to that of bulk polycrystalline platinum, for the oxygen reduction reaction.[27] Here, we demonstrate the extended capacity of this vapor deposition method for the synthesis and thermal evolution of bimetallic nanostructures by detailing the synthesis of platinum−ruthenium nanotubes.

To date, platinum−ruthenium catalysts have been the preferred choice of anode catalyst for direct methanol fuel cells (DMFCs).[28] Although Pt is the only catalytically active component of Pt−Ru alloys for methanol oxidation, a bare Pt surface is readily covered by the reaction intermediate carbon monoxide ($CO_{ads}$). In order to remove adsorbed CO from Pt sites on bare Pt catalysts, oxygen-containing species like hydroxide must form on adjacent sites to oxidize $CO_{ads}$ to $CO_2$.[29−32] The formation of oxygen-containing species on Pt is delayed until high potentials, leaving Pt surfaces blocked by adsorbates beyond the desirable window for DMFC operation.[33] In the presence of ruthenium in a PtRu alloy, Pt adsorbs and dehydrogenates methanol in consecutive steps until a surface-adsorbed CO-like species remains on the surface Pt sites, which is oxidized by the oxygen-containing species that form on Ru at lower potentials relative to Pt,[34] a process known as the bifunctional mechanism.[35−38]

Metallic PtRu alloys have been the most-studied DMFC anode catalyst,[28] but other promising mixed-phase Pt−Ru catalysts have emerged featuring the hydrous oxide phase of Ru ($RuO_xH_y$) with metallic Pt. The promotional effects of Ru on Pt for CO oxidation are closely linked to its oxidation state. The hydrous oxide of Ru weakens the Pt interaction with CO while providing OH adsorption locations for CO oxidation.[39] The presence of the hydrous oxide as the exclusive Ru species in a Pt−Ru catalyst was shown to enhance methanol oxidation activity by 2 orders of magnitude compared to the metallic and anhydrous forms.[36] The methanol oxidation activity enhancement by hydrous ruthenium oxide has been attributed to its mixed valence, its ability to conduct protons and electrons, and its natural expression of Ru−OH.[36]

This work showcases the potential of this metalorganic vapor deposition technique by detailing the synthesis of two distinct types of platinum−ruthenium nanotubes. In the as-synthesized case, nanotubes are synthesized with walls composed of a nominally bilayered structure comprising an interior of bulk hydrous Ru oxide and an exterior of metallic Pt. In this catalyst motif, which has been deployed previously with different extended nanostructures and materials for other reactions,[40−45] catalytically active Pt decorates the surface of the nanotube and is highly utilized, while the more abundant and less expensive Ru provides structural support, composing the wall interiors. In the second case, the layered Pt−Ru nanotubes are annealed while still within the template to reduce the hydrous oxide to metallic Ru and to promote nanotube wall porosity, grain growth, and Pt−Ru alloy formation. In each case, the template is etched away to yield unsupported, dispersed nanotube suspensions.

## 2. MATERIALS AND METHODS

Platinum−ruthenium nanotubes were synthesized by consecutive vapor deposition experiments, each consisting of the deposition of one metal species. Platinum was deposited first, followed by deposition of ruthenium, within the pores of an anodic alumina (AAO) membrane (Whatman Anodisc, 13 mm diameter, 200 nm pore size). A powder of platinum(II) 2,4-pentanedionate (Alfa Aesar), or platinum acetylacetonate, was contained beneath the porous alumina template and transferred to a vacuum oven with a glass vial containing 2.3 mL of DI water. The oven was evacuated with a rotary vane vacuum pump and purged with dry $N_2$ several times before finally being evacuated to 0.3 bar and sealed. The oven thermostat was set to a calibrated value of 180 °C. The liquid water was vaporized and equilibrium was reached after 75 min at a total pressure of 0.8 bar, as measured by a Bourdon gauge. The oven was evacuated after 15 h at 180 °C, flushed with dry $N_2$, and cooled to room temperature before the Pt-bearing template was recovered, and the mass of Pt deposited during this first step of the synthesis was measured.

The above procedure for platinum deposition was repeated at an elevated temperature for the deposition of ruthenium within the Pt-seeded template. Hydrous ruthenium oxide [$Ru(O_xH_y)$] was deposited along the Pt-lined channels of the alumina template from the decomposition of ruthenium(III) 2,4-pentanedionate at 240 °C. By adjusting the masses of the respective precursor doses, the masses of Pt and $Ru(O_xH_y)$ that were deposited sequentially were controlled, from which the nanotube sample composition was determined.

The platinum- and hydrous ruthenium oxide-filled templates were then immediately dissolved or thermally annealed to induce morphological and chemical phase changes and alloy formation. The sample templates were annealed in a quartz tube furnace with a flowing $H_2$ (4% hydrogen, balance argon) mixture. After purging the furnace tube for 30 min, the templates were heated at 750 °C for 1 h before they were allowed to cool passively to room temperature.

To liberate the nanotubes for further study, the sacrificial alumina templates were dissolved by magnetic stirring in 30% KOH solution at room temperature for 90 h. The supernatant solution was then decanted and replaced with deionized water, a process that was repeated until the pH of the supernatant solution was neutral. A variety of characterization techniques were then used to analyze the structure, morphology, and chemistry of the as-synthesized and heat-treated nanotubes. Scanning electron microscopy (SEM) images were acquired using a ZEISS 1525 field emission SEM using an accelerating voltage of 3 kV and an in-lens electron detector. SEM-EDS measurements of nanotube chemical compositions were acquired at an accelerating voltage of 20 kV. A Hitachi NB-5000 focused ion beam (FIB) instrument was used to prepare thin TEM cross sections of samples still in the AAO template for scanning transmission electron microscopy (S/TEM) imaging and EDS mapping using a JEOL 2200FS operating at 200 kV. High-resolution (HRTEM) images were acquired on these FIB-derived lamellae using a FEI Titan S/TEM


DOI: 10.1021/am508228b
ACS Appl. Mater. Interfaces 2015, 7, 10115−10124

operating at 300 kV. X-ray photoelectron spectroscopy (XPS) data were collected using a PHI 3056 spectrometer with an Al anode source operated at 15 kV and an applied power of 350 W. No charge correction was required or applied. High-resolution data were collected at a pass energy of 23.5 eV with 0.05 eV step sizes and a minimum of 50 scans to improve the signal-to-noise ratio; lower-resolution survey scans were collected at a pass energy of 93.5 eV with 0.5 eV step sizes and a minimum of 20 scans. XRD patterns were measured with a Bruker D2 Phaser diffractometer with Cu K$\alpha$ radiation ($\lambda$ = 0.154 187 4 nm, 30 kV, 10 mA, 0.014° step, 0.5 s/step).

Electrode inks were prepared for electrochemistry experiments by diluting the nanotube–water suspensions to concentrations ranging from 0.25 to 0.50 $mg_{PtRu}$ $mL^{-1}$. No alcohol or ionomer was added to the inks. The unsupported platinum–ruthenium nanotubes were deposited on the working electrode with loadings of 25–60 $\mu g_{PtRu}$ $cm^{-2}_{elec}$.

Cyclic voltammetry (CV) measurements were performed in a glass electrochemical cell with a glassy carbon (GC) working electrode, platinum wire counter electrode, and $Hg/Hg_2SO_4$ (0.5 M $H_2SO_4$) reference electrode. All potentials reported in this work are referred to a reversible hydrogen electrode (RHE) by calibration of the reference electrode versus a Pt electrode in hydrogen-saturated electrolyte. Prior to applying catalyst inks to the GC electrode, solids in the inks were dispersed by sonication in an ice bath for 20 min. A 10 $\mu$L aliquot of catalyst ink was applied to the GC and allowed to dry in air at room temperature.

Prior to each experiment, the electrolyte was deoxygenated by purging with ultrahigh purity $N_2$ gas for at least 30 min. The electrodes were conditioned at the start of each experiment with 15 cycles in 0.5 M $H_2SO_4$ (Alfa Aesar, 99.9999% metals basis) from 0.05 to 0.70 V vs RHE at 100 mV $s^{-1}$. Subsequent to conditioning, three additional cycles were recorded at 20 mV $s^{-1}$.

Carbon monoxide (CO) stripping voltammetry was performed in 0.5 M $H_2SO_4$. The electrolyte was saturated with CO and a potential of 0.1 V was applied to the working electrode to adsorb CO. The applied potential was maintained while the electrolyte was purged with 4% CO (balance Ar) for an additional 10 min followed by purging with nitrogen for 30 min. CO stripping voltammograms were recorded in the nitrogen-purged electrolyte at 20 mV $s^{-1}$. Electrochemically active surface areas (ECSAs) were calculated using the charge for removing a monolayer of CO from a Pt surface (420 $\mu$C $cm^{-2}$).[46] Methanol oxidation reaction (MOR) activity was measured by cycling the electrode in fresh 0.5 M $CH_3OH$ (Fisher Scientific, HPLC grade) and 0.1 M $H_2SO_4$ from 0.05 to 1.2 V vs RHE at 20 mV $s^{-1}$. ECSAs obtained during CO stripping voltammetry were used to normalize methanol oxidation linear sweep voltammograms to catalyst surface area. Platinum–ruthenium black (Alfa Aesar, nominally 50% atomic Pt) was used to benchmark the performance of the experimental catalysts. Preparation of the catalyst ink and electrodes prepared with the commercial catalyst followed the procedures outlined above for the experimental catalysts.

## 3. RESULTS AND DISCUSSION

Representative SEM images of as-synthesized Pt-decorated, hydrous Ru oxide nanotubes [PtRu($O_xH_y$)NTs] and annealed, alloyed platinum–ruthenium nanotubes (PtRuNTs) are presented in Figure 1. In each case, the initial deposition of Pt nanoparticles within the anodic alumina template lined the template channels before a successive layer of hydrous Ru oxide was deposited, which would become the interior of the nanotube upon dissolution of the template. The presence of Pt within the template enhanced the efficiency of the Ru deposition by 5 times in comparison to a Pt-free template, indicating that Pt catalyzed the deposition of Ru within the pores of the AAO membrane. Individual nanotubes maintained morphologies similar to the shapes of the pores of the templates in which they were vapor-deposited. The nanotube

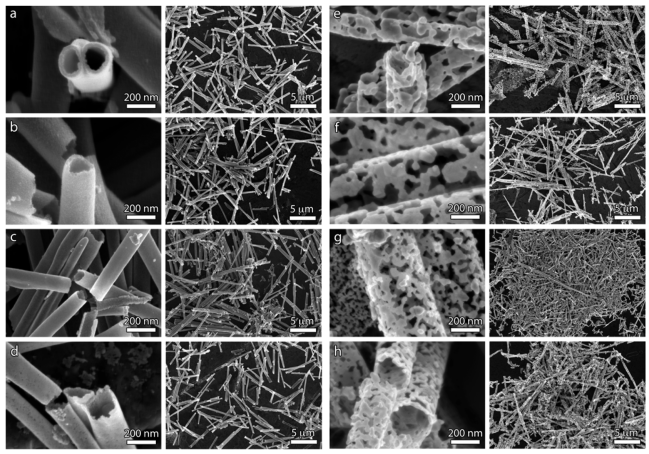


**Figure 1.** SEM images of as-synthesized PtRu($O_xH_y$)NTs: (a) 10% Pt, (b) 17% Pt, (c) 38% Pt, and (d) 64% Pt. SEM images of PtRuNTs annealed at 750 °C in 4% $H_2$: (e) 9% Pt, (f) 20% Pt, (g) 47% Pt, an (h) 60% Pt.

cross sections are roughly circular and approximately 200 nm in diameter, with lengths ranging from 2 to 50 $\mu$m.

SEM images of the as-synthesized PtRu($O_xH_y$)NTs are presented in Figure 1a–d at high and low magnifications. Owing to the conformal nature of the initial Pt deposit within the channels of the alumina template, the exterior surfaces of the as-synthesized nanotubes are uniform with no noticeable porosity. The interiors of the nanotubes are composed of a conformal hydrous Ru oxide layer that was vapor-deposited on the interiors of the Pt-lined AAO channels in a second vapor deposition step. The respective thicknesses of the Pt and Ru($O_xH_y$) layers vary with the amounts of each material deposited during synthesis and are controlled in order to achieve nanotubes of desired chemical compositions. Following a heat treatment at 750 °C for 1 h in 4% $H_2$, the PtRuNTs in Figure 1e–h displayed structural and chemical evolution. The initially nanoparticulate and finely textured Pt exterior of the PtRu($O_xH_y$)NTs evolved to a more coarsely grained, highly porous, and smooth surface. The more-Pt-rich, alloyed nanotubes (Figure 1g,h) experienced less grain growth than the Ru-rich nanotubes, resulting in tube walls with a finer, filigree-like structure, rather than the globular, beadlike walls of the Ru-rich $Pt_9Ru_{91}$NTs in Figure 1e. The differences in the observed mesostructures with varying Pt–Ru content may be influenced by disparities in self-diffusion rates in the nanostructured walls and the energetics of the nanotube surface interaction with the AAO template.

To better understand the structural and chemical evolution of the nanotubes from the as-synthesized PtRu($O_xH_y$)NTs to the annealed PtRuNTs, cross sections were prepared from 58% Pt nanotubes that were left intact and within the $Al_2O_3$ template. Figure 2 shows representative HAADF STEM images and EDS elemental mapping of the nanotubes within the AAO pore walls for the as-synthesized PtRu($O_xH_y$)NTs (Figure 2a–f) and PtRuNTs following heat treatment at 750 °C (Figure 2g–l). For the case of the as-synthesized PtRu($O_xH_y$)NTs, HAADF STEM imaging (Figure 2a) and EDS mapping show the elemental distribution of Al and O in the $Al_2O_3$ pore walls (Figure 2b,c) and the conformal coatings of Pt (Figure 2d) and Ru (Figure 2e) that line the $Al_2O_3$ pore walls. Moreover, the composite STEM–EDS map (Figure 2f) shows a thin layer of elemental Pt at the $Al_2O_3$ pore wall interface, which is to be


DOI: 10.1021/am508228b
ACS Appl. Mater. Interfaces 2015, 7, 10115–10124

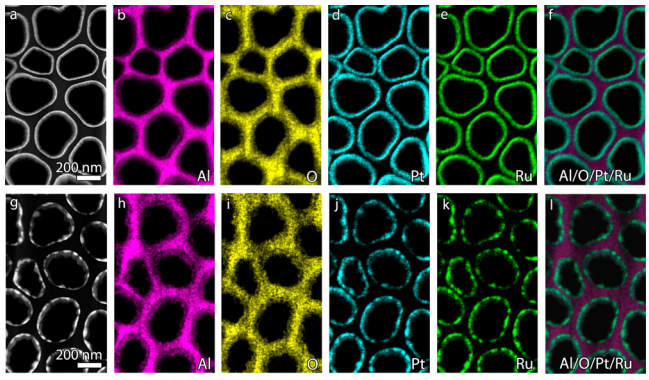


**Figure 2.** HAADF STEM and EDS elemental mapping of (a–f) as-synthesized $Pt_{58}Ru_{42}(O_xH_y)$NTs and (g–l) annealed, alloyed $Pt_{58}Ru_{42}$NTs at 750 °C in 4% $H_2$ for 1 h. Cross sections were observed by leaving the nanotubes embedded within the sacrificial AAO template.

expected since platinum was first deposited within the $Al_2O_3$ pore walls prior to Ru deposition. Following heat treatment at 750 °C for 1 h in 4% $H_2$, the morphology of the PtRuNT no longer remains conformal; rather, the PtRuNT coating along the $Al_2O_3$ pore wall is highly nonuniform, as can be seen in the HAADF STEM image in Figure 2g, which can be correlated with the porous nature of the PtRuNT following heat treatment that is observed in Figure 1e–h. There is no indication of elemental segregation between Pt (Figure 2j) and Ru (Figure 2k) along the $Al_2O_3$ pore wall (Figure 2h,i), indicating that Pt and Ru alloyed during exposure to the 4% $H_2$ environment at 750 °C. Further characterization of the nanotubes can be seen in high-resolution TEM (HRTEM) images in Figure 3. For the as-synthesized $PtRu(O_xH_y)$NTs, the TEM images in Figure 3a,b further reveal the conformal coating nature of the nanotube while still in the $Al_2O_3$ template, but they also

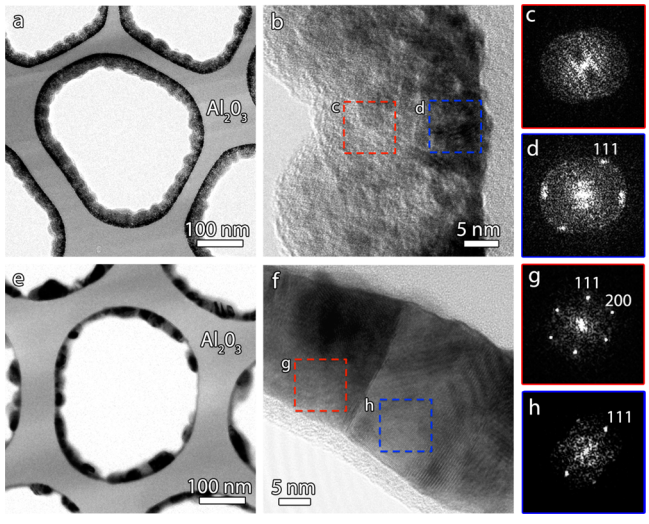


**Figure 3.** TEM images of the (a, b) as-synthesized $Pt_{58}Ru_{42}(O_xH_y)$-NTs showing the amorphous $Ru(O_xH_y)$ layer on nanocrystalline Pt lining the $Al_2O_3$ pore walls. FFT analysis from the boxed regions in part b correspond to (c) amorphous $Ru(O_xH_y)$ and (d) crystalline Pt. The TEM images in parts e and f are from the annealed $Pt_{58}Ru_{42}$NTs and show PtRu nanocrystals. FFT analyses from the boxed regions in part f correspond to a PtRu crystal oriented along (g) the [011] zone axis and (h) the (111) lattice planes.

show the amorphous layer of $Ru(O_xH_y)$ deposited onto Pt nanoparticles that lines the walls of the template channels, which is confirmed through fast Fourier transform (FFT) analysis in Figure 3c,d, respectively. Following heat treatment at 750 °C for 1 h in 4% $H_2$ (Figure 3e–h), the TEM images reveal how $PtRu(O_xH_y)$ is transformed into individual, PtRu nanocrystals, as shown in Figure 3e,f. FFT analysis from the boxed regions in Figure 3f reveals that the structures of the PtRu crystals have a face-centered cubic crystal structure. The FFT in Figure 3g shows a region of the crystal that is oriented along the [011] zone axis, and the crystal to the right (Figure 3h) shows the (111) lattice planes.

The observed increase in grain size induced by the heat treatment is confirmed by Scherrer analysis of the X-ray diffraction patterns in Figure 4. The as-synthesized nanotubes

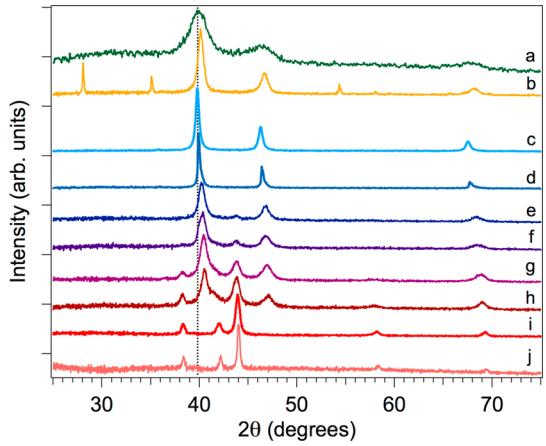


**Figure 4.** Cu K$\alpha$ X-ray diffraction patterns of (a) as-synthesized $Pt_{64}Ru_{36}(O_xH_y)$NT, (b) $Pt_{60}Ru_{40}O_x$NT annealed at 750 °C in $N_2$, and nanotubes annealed at 750 °C in $H_2$: (c) PtNT, (d) $Pt_{80}Ru_{20}$NT, (e) $Pt_{64}Ru_{36}$NT, (f) $Pt_{60}Ru_{40}$NT, (g) $Pt_{43}Ru_{57}$NT, (h) $Pt_{38}Ru_{62}$NT, (i) $Pt_7Ru_{93}$NT, and (j) RuNT.

(Figure 4a) contain relatively broad face-centered cubic (fcc) peaks in comparison to the annealed $Pt_{64}Ru_{36}$NTs (Figure 4e) of the same composition. Scherrer widths of the Pt(111) peaks for the two samples were calculated to quantify the change in grain size, and an increase in grain size from 4.1 nm for the as-synthesized sample to 11.8 nm in the annealed sample was observed.

The diffraction pattern of as-synthesized $Pt_{64}Ru_{36}(O_xH_y)$NTs (Figure 4a) only contains peaks corresponding to the fcc geometry of the Pt unit cell. There is no shift in the location of the Pt(111) peak that would indicate the formation of a PtRu alloy during synthesis and prior to high-temperature annealing. The lack of characteristic peaks of tetragonal anhydrous ruthenium oxide ($RuO_2$) or hexagonal close-packed (hcp) peaks of metallic Ru suggests that a hydrous oxide of Ru, which is amorphous,[47,48] was formed during synthesis. Diffraction patterns of more $PtRu(O_xH_y)$NTs are located in Figure S1 of the Supporting Information, which illustrate the amorphous nature of the as-synthesized hydrous Ru oxide nanotubes with variable Pt content. During heat treatment at 750 °C in inert gas, in this case $N_2$, the structural water is removed and crystalline, anhydrous Ru oxide is formed (Figure 4b), which exhibits a diffraction pattern distinct from that of metallic Ru. In a forming gas environment, hydrous Ru oxide was reduced to metallic Ru in our annealed, pure ruthenium nanotubes


DOI: 10.1021/am508228b
ACS Appl. Mater. Interfaces 2015, 7, 10115–10124

(RuNTs, Figure 4j). Nanotubes composed of hydrous Ru oxide and metallic Ru were the focus of this study of methanol oxidation.

The diffraction patterns in Figure 4 indicate the formation of alloys during heat treatment at 750 °C. As the composition of the annealed nanotube samples departs from monometallic Pt (Figure 4c) to feature a small amount of Ru (Figure 4d), the Pt(111) peak shifts to higher values of $2\theta$; the Pt lattice contracts as Ru, with smaller atomic radius than Pt, substitutes into the Pt lattice.[49] The dashed line in Figure 4 corresponds to the lattice parameter of the Pt(111) peak in bulk polycrystalline platinum. The lattice contraction of the PtRuNTs increased with the increase in Ru content (Figure 4d–i). In nanotube samples with Ru composition between 36 and 62%, the formation of a dual-phase alloy is observed. Characteristic hcp peaks of metallic Ru emerge and intensify with increasing Ru content in the nanotubes. The formation of fcc and hcp alloy phases at compositions closer to a 1:1 atomic ratio of Pt to Ru is believed to be a result of the relatively thick layers of Pt and hydrous Ru oxide sequentially deposited to compose the nanotube walls during synthesis that are discernible in the HAADF STEM and TEM images of the as-synthesized $Pt_{58}Ru_{42}(O_xH_y)$NTs. When the Ru composition is increased to 93% (Figure 4i), a homogeneous PtRu alloy is formed, as evidenced by the pure hcp phase. In this case, the Pt layer at the nanotube exterior is assumed to be very thin and all Pt present has diffused into the Ru lattice.

A more detailed probing of nanotube chemical composition and the transformations induced during the heat treatment is possible using XPS analysis. A composition near the midpoint of the examined range was selected (nominally $Pt_{59}Ru_{41}$). As-synthesized and heat-treated samples of this composition were drop-cast from water solutions on Si wafers after dissolution of the AAO template. PtRu black was similarly prepared. High-resolution XPS scans of the Pt 4f doublet and the Ru $3p_{3/2}$ peak, along with peak deconvolution components derived via nonlinear least-squares fitting, are shown in Figure 5. In the case of the Pt $4f_{7/2}$ and $4f_{5/2}$ peaks, components were fixed in a 3:4 ratio with ~3.5 eV peak separations. Additional scans are available in the Supporting Information (Figure S3). In both of the experimental nanotube samples, Pt is present almost entirely as metallic Pt, with a small amount of $Pt^{2+}$ and $Pt^{4+}$ discernible. The PtRu black sample exhibits more oxidized Pt, clearly visible in the elevation of the Pt $4f_{5/2}$ peak above the Pt $4f_{7/2}$ one in Figure 5c.

Ru is present primarily as metallic Ru in the annealed nanotube sample, with a small amount of $Ru^{4+}$ present, presumably as $RuO_2$. The presence of this oxide can be inferred from the HRTEM images in Figure 3f, which show what may be a 1–2 nm oxide film on the tube interior. Some degree of oxidation is also inferred from edge shifts observed in Ru K-edge XANES (Figure S2, Supporting Information). In the case of the as-synthesized nanotube sample, the Ru signal was of very low intensity and thus exhibited significant noise (Figure 5e). In addition to any chemical information, we are also able to infer supporting structural information from the low intensity of this peak. As we observed in our HRTEM investigations, Ru is initially confined to the nanotube interiors. In the case of moderate Pt content, Pt dominates the outer surfaces of the nanotubes freed from the AAO template and acts to absorb the scattered Ru photoelectrons. The surface composition measured by XPS peak areas adjusted via the appropriate atomic adsorption factors was approximately 10:1 Pt:Ru in the case of the as-synthesized sample. Using the same analysis of the annealed sample returned the nominal composition measured via EDS.

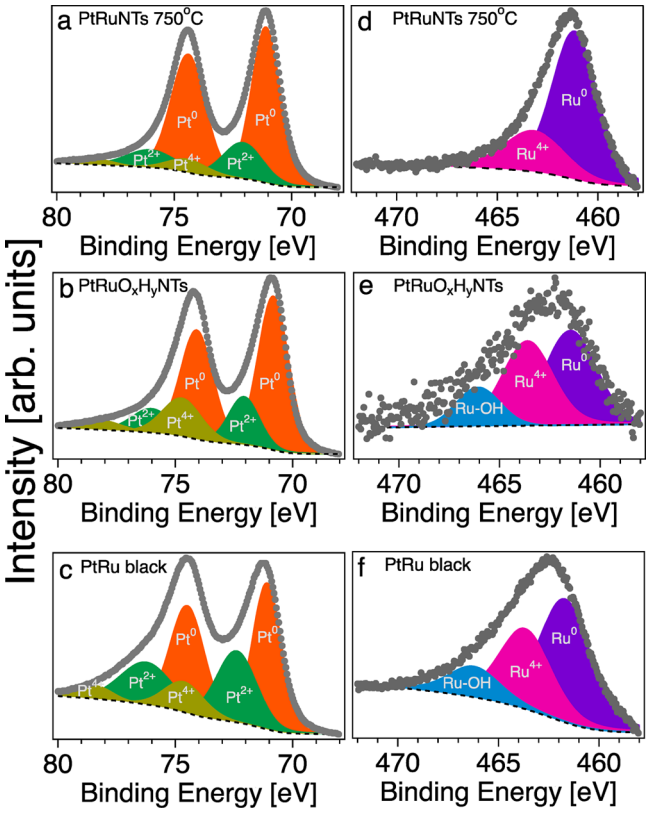


**Figure 5.** High-resolution XPS spectra of the Pt 4f doublet (a–c) and the Ru $3p_{3/2}$ peak (d–f) for (a, d) 750 °C, 4% $H_2$-annealed $Pt_{59}Ru_{41}$NTs, (b, e) as-synthesized $Pt_{59}Ru_{41}(O_xH_y)$NTs, and (c, f) PtRu black.

Deconvolution of the as-synthesized Ru $3p_{3/2}$ peak found almost equal amounts of metallic Ru and $Ru^{4+}$ species, with approximately 15% of the total observable Ru present as $RuO_xH_y$-type species. However, we stress that this is not the overall Ru chemical composition but rather the Ru species located closest to the walls of the tubes. Analysis of the PtRu black Ru $3p_{3/2}$ peak reveals a similar 1:1 balance of metallic to $Ru^{4+}$ species, though 13% of the Ru in this case is present as Ru hydrates. Of course, under potential control in aqueous media, we expect interconversion of the metallic and crystalline oxides to the hydrous forms in the case of all samples.

In Figure 6A, the cyclic voltammograms in acid of as-synthesized $PtRu(O_xH_y)$NTs further demonstrate that ruthenium is deposited as a hydrous oxide during synthesis and prior to heat treatment. As the Ru content in the nanotubes is increased relative to Pt, the characteristic hydrogen adsorption and desorption regions (0.05–0.35 V vs RHE) diminish and the capacitive features associated with the mixed-valent, hydrous oxide of Ru dominate the voltammograms.[50] The high specific capacitance observed here is attributed to the ability of hydrous ruthenium oxide to transport and store electrons and protons.[34,48] The dashed line in Figure 6A represents reduced, metallic ruthenium nanotubes (RuNTs). The versatility of this synthesis technique is highlighted by Figure 6B, which features cyclic voltammograms of three different nanotube sample types with low Pt content, each with a unique chemical phase of ruthenium. The above-mentioned


DOI: 10.1021/am508228b
ACS Appl. Mater. Interfaces 2015, 7, 10115–10124

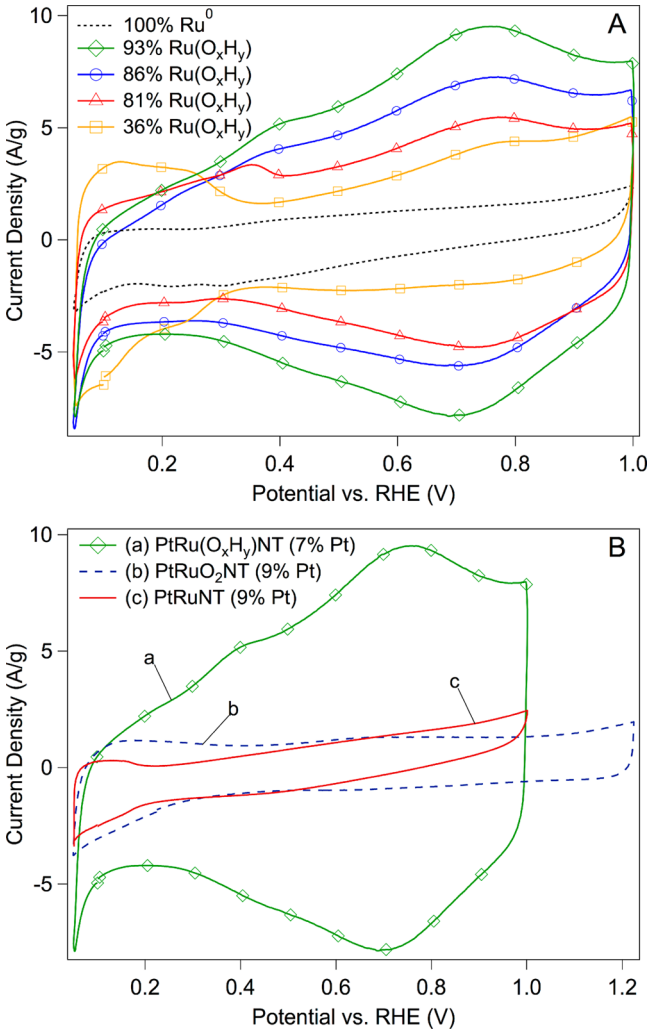


**Figure 6.** Cyclic voltammograms recorded in 0.5 M $H_2SO_4$ at 20 mV $s^{-1}$. In part A, pure and metallic RuNTs (dashed black line) which are reduced at 750 °C in 4% $H_2$ are compared to as-synthesized PtRu($O_xH_y$)NTs with variable Pt content. In part B, (a) as-synthesized PtRu($O_xH_y$)NTs, (b) 750 °C $N_2$-annealed $PtRuO_2$NTs, and (c) 750 °C, 4% $H_2$-annealed PtRuNTs with similar Pt content are compared.

as-synthesized nanotubes that feature amorphous, hydrous Ru oxide are compared to two PtRuNT samples that are annealed in different gas environments. The Pt and anhydrous, crystalline Ru oxide ($RuO_2$) nanotubes [Figure 6B(b)] were prepared by annealing in dry nitrogen at 750 °C. Like the alloyed PtRuNTs [Figure 6B(c)] that feature metallic Ru after a heat treatment in 4% $H_2$ at 750 °C, the anhydrous and crystalline ruthenium oxide is relatively featureless in the capacitive charging region in comparison to the hydrated form of the Ru oxide.

Methanol oxidation specific activities of the experimental nanotube catalysts are plotted against their Pt composition in Figure 7. At all quantities of Pt content tested for the experimental catalysts, the as-synthesized PtRu($O_xH_y$)NTs are more active than their annealed counterparts, because they have the highest degree of Pt utilization and Ru is present in its hydrous oxide form. In the as-synthesized nanotubes (Figure 7, red squares), it must be considered that these samples are composed of a hydrous Ru oxide interior with a discrete Pt surface layer, as demonstrated in the TEM images in Figure 3a–d, with the latter increasing in thickness with Pt content. Therefore, the concept of Pt content must be considered

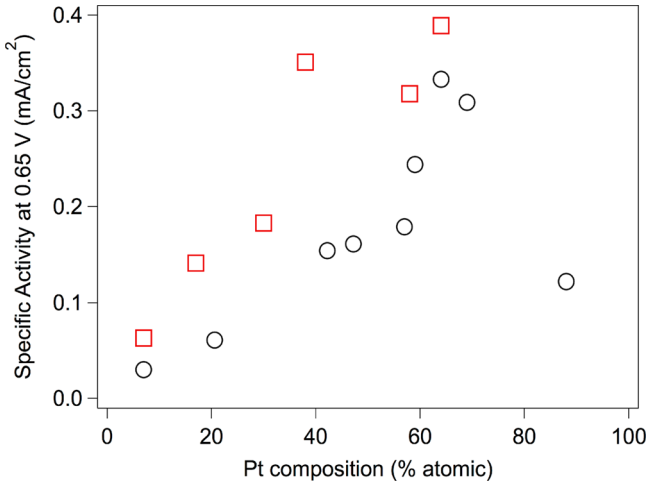


**Figure 7.** Scatter plot of specific activity vs Pt content measured at 0.65 V vs RHE for as-synthesized PtRu($O_xH_y$)NTs (red squares) and alloyed PtRuNTs (black circles) recorded in 0.5 M $CH_3OH$ and 0.1 M $H_2SO_4$.

differently from that of the alloyed PtRuNTs (Figure 7, black circles), where a consideration of bulk composition applies. When more-Ru-rich, the specific activities of the PtRu($O_xH_y$)-NTs increase almost linearly with Pt content from 7% to 38% Pt, as more catalytically active Pt is effectively added to the nanotube exterior in a thin and conformal Pt layer. In the more-Pt-rich PtRu($O_xH_y$)NTs (40–64% Pt), the core–shell design is most effective and the specific activity no longer increases with Pt content, but rather plateaus, as the nanotube exterior surfaces become more enriched with Pt, as is visible in the representative HAADF STEM (Figure 2a–f) and TEM images (Figure 3a–d) of $Pt_{58}Ru_{42}$($O_xH_y$)NTs. Similarly in the alloyed PtRuNTs, the specific activity increases with Pt composition until a maximum activity is observed at 64% Pt, followed by a reduction in activity in the most-Pt-rich samples. We suggest that the $Pt_{64}Ru_{36}$NTs are the most active of the alloyed nanotubes, because they are well-dispersed with a high degree of surface Pt–Ru pair sites that are required to remove methanol oxidation intermediates from their surfaces efficiently, as manifested by their CO stripping voltammograms. Both nanotube sample types reported maximum specific activities at 64% Pt content, and these particular samples have been isolated for further study. Low-Pt-content, as-synthesized $Pt_{17}Ru_{83}$($O_xH_y$)NTs with a presumably thin Pt surface layer are also highlighted, because they may serve as a better model of their core–shell design.

CO stripping voltammograms are shown in Figure 8. The charge of a respective sample's CO stripping peak was used to determine the catalyst's electrochemical surface area (ECSA), which is reported in Table 1 and is used to normalize the mass-normalized voltammograms in Figure 8A to the area-normalized voltammograms in Figure 8B. Commercial PtRu black (Figure 8a) is a highly dispersed alloy of Pt and Ru with high ECSA that efficiently oxidizes surface-adsorbed CO at relatively low potentials due to its high degree of metal dispersion and alloying. The alloyed $Pt_{64}Ru_{36}$NT sample had an earlier onset and lower peak potential for CO oxidation than both of the as-synthesized nanotube samples, which is the result of an improved dispersion of Pt and Ru and the concomitant increase of bimetallic Pt–Ru pair sites. Additionally, the increased grain size of the annealed $Pt_{64}Ru_{36}$NTs is expected


DOI: 10.1021/am508228b
ACS Appl. Mater. Interfaces 2015, 7, 10115–10124

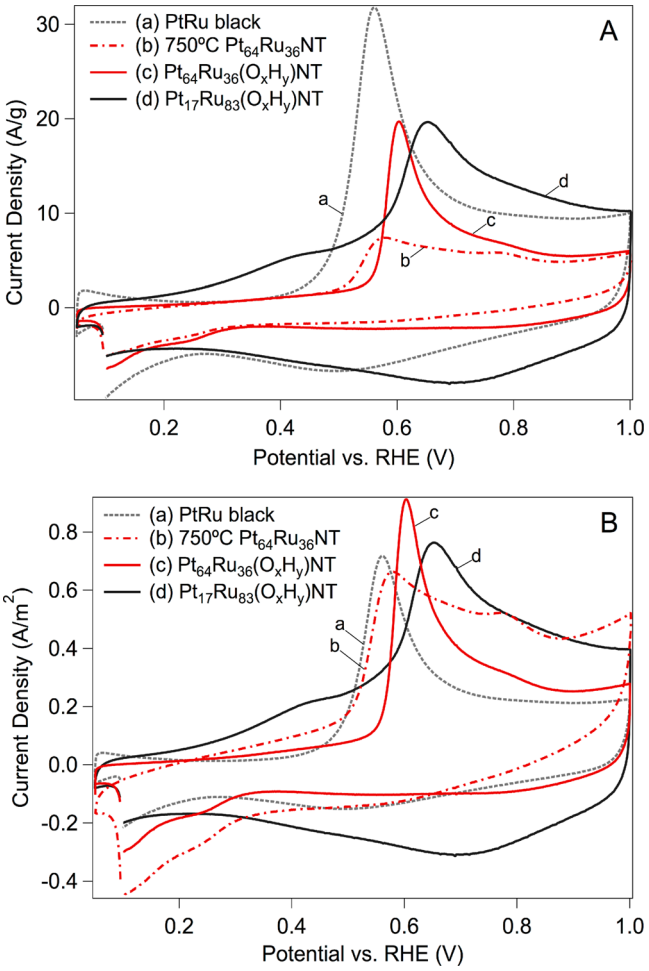


**Figure 8.** CO stripping voltammograms recorded in 0.5 M $H_2SO_4$ at 20 mV $s^{-1}$ normalized to (A) total electrode mass and (B) ECSA. CO was adsorbed at 0.1 V vs RHE.

to promote faster $CO_{ads}$ oxidation, likely from an increase in CO surface diffusion expected on the surface of a larger nanoparticle.[33,51,52] However, the CO stripping peak of the alloyed PtRuNT (Figure 8b) is broad and features a shoulder at higher potentials (0.77 V) that presumably corresponds to more-Pt-rich regions at the surfaces of the nanotubes that are less active for CO oxidation.

Though the phase of Ru varies between the as-synthesized and annealed Pt−Ru nanotube samples, the change in CO stripping kinetics is more likely dependent on the proximity of Pt to Ru in the catalyst.[53] The bifunctional mechanism that is used to explain methanol oxidation on a Pt−Ru catalyst maintains that adsorbed CO is produced at the Pt sites while Ru provides oxygenated species to assist in oxidizing the adsorbed intermediate. The putative Pt and $Ru(O_xH_y)$ layers in the as-synthesized $PtRu(O_xH_y)$NTs lack the proximity between Pt and Ru necessary for improved CO stripping kinetics.[54] In this case of distinct material layers with less uniform dispersion of Pt and Ru than in an alloy, there is a greater diffusional distance required of Pt-adsorbed CO to migrate along the catalyst surface to the Ru for CO oxidation and desorption from the catalyst surface.[36,38]

Figure 9 shows linear sweep voltammograms for methanol oxidation with currents normalized to total catalyst mass (Figure 9A) and ECSA (Figure 9B). Despite an observed decline in CO stripping kinetics, the as-synthesized $PtRu(O_xH_y)$NT samples are surprisingly active for methanol oxidation. This is an interesting, although not unique, result considering that CO-like intermediates are formed during the methanol oxidation reaction and a sample that oxidizes CO effectively is expected to be more active for methanol oxidation. However, CO oxidation does not necessarily correlate to methanol oxidation activity[53] and the $Pt_{64}Ru_{36}(O_xH_y)$NTs have a comparable mass activity to PtRu black at 0.7 V vs RHE despite half the ECSA. The high activity of the $Pt_{64}Ru_{36}(O_xH_y)$NTs can be ascribed to its high Pt utilization and the presence of hydrous Ru oxides in similarity with PtRu black.[55] This can be seen in the XPS scans of the Ru $3p_{3/2}$ peak (Figure 5) and

**Table 1. Location of Pt(111) Peak, Crystallite Size ($L$) Measured by Scherrer Analysis of the Pt(111) Peak, Electrode Loading, Electrochemical Surface Area (ECSA), MOR Mass and Specific Activities, and MOR Pt Mass and Pt Specific Activities at 0.65 V vs RHE**

| Sample | Pt(111) 2$\theta$ (deg) | $L$ (nm) | loading ($\mu g/cm^2_{disk}$) | ECSA ($m^2/g$) | $i_m$ (A/g) | $i_s$ ($mA/cm^2$) | Pt $i_m$ ($A/g_{Pt}$) | Pt $i_s$ ($mA/cm^2_{Pt}$) |
|---|---|---|---|---|---|---|---|---|
| PtRu black | 40.342 | 2.8 | 55.78 | 44.3 | 96 | 0.217 | 146.3 | 0.330 |
| $Pt_7Ru_{93}O_xH_y$NT | | | 68.33 | 14.4 | 9 | 0.063 | 70.9 | 0.497 |
| $Pt_{17}Ru_{83}O_xH_y$NT | 39.717 | 3.9 | 36.42 | 25.8 | 36 | 0.141 | 127.1 | 0.498 |
| $Pt_{30}Ru_{70}O_xH_y$NT | | | 26.13 | 20.7 | 38 | 0.183 | 83.9 | 0.404 |
| $Pt_{38}Ru_{62}O_xH_y$NT | | | 28.25 | 24.8 | 87 | 0.351 | 160.5 | 0.648 |
| $Pt_{58}Ru_{42}O_xH_y$NT | 39.763 | 3.8 | 29.36 | 33.6 | 107 | 0.318 | 147.1 | 0.437 |
| $Pt_{64}Ru_{36}O_xH_y$NT | 39.813 | 4.1 | 31.33 | 21.6 | 84 | 0.389 | 108.5 | 0.502 |
| $Pt_7Ru_{93}$NT | | 33.8 | 36.88 | 9.9 | 3 | 0.030 | 23.6 | 0.236 |
| $Pt_{21}Ru_{79}$NT | | 27.6 | 43.20 | 6.9 | 4 | 0.061 | 11.8 | 0.180 |
| $Pt_{39}Ru_{61}$NT | 40.568 | 12.0 | 40.75 | | 13 | | 23.5 | |
| $Pt_{42}Ru_{58}$NT | 40.503 | 9.2 | 53.34 | 6.8 | 11 | 0.154 | 18.9 | 0.279 |
| $Pt_{47}Ru_{53}$NT | 40.437 | 13.7 | 42.03 | 6.1 | 10 | 0.161 | 15.8 | 0.276 |
| $Pt_{51}Ru_{49}$NT | 40.421 | 11.9 | 39.07 | | 18 | | 27.0 | |
| $Pt_{57}Ru_{43}$NT | 40.326 | 9.7 | 42.79 | 7.8 | 14 | 0.179 | 19.3 | 0.268 |
| $Pt_{59}Ru_{41}$NT | 40.301 | 9.7 | 48.24 | 8.7 | 22 | 0.244 | 30.3 | 0.336 |
| $Pt_{64}Ru_{36}$NT | 40.238 | 11.8 | 38.21 | 9.0 | 30 | 0.333 | 38.7 | 0.430 |
| $Pt_{69}Ru_{31}$NT | 40.142 | 9.1 | 40.75 | 9.4 | 29 | 0.309 | 35.8 | 0.381 |
| $Pt_{88}Ru_{12}$NT | 39.937 | 16.3 | 45.85 | 9.3 | 11 | 0.118 | 11.8 | 0.126 |


DOI: 10.1021/am508228b
ACS Appl. Mater. Interfaces 2015, 7, 10115−10124

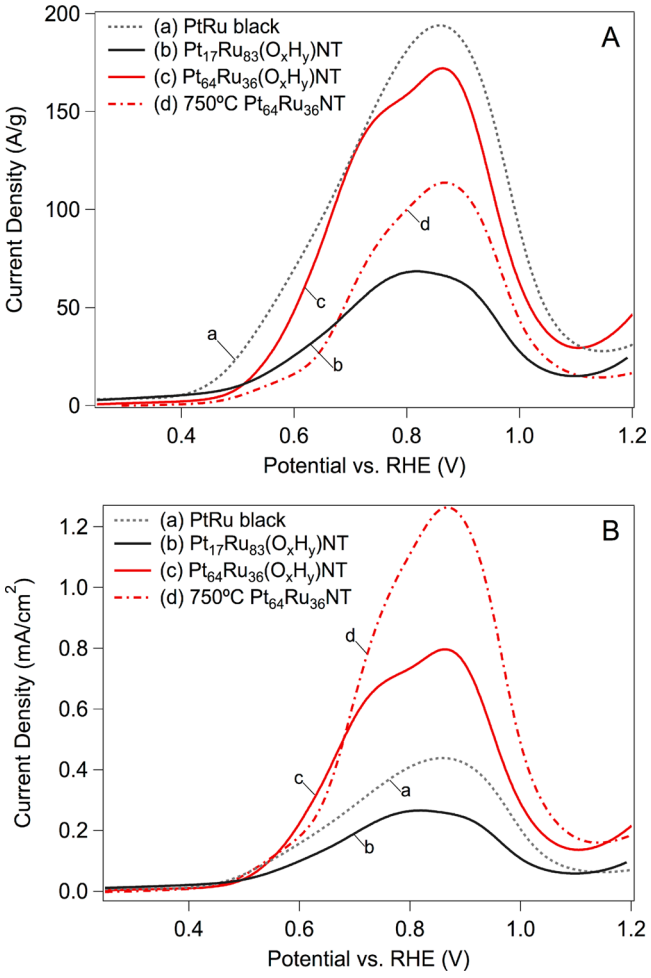


**Figure 9.** Linear sweep voltammograms recorded in 0.5 M $CH_3OH$ and 0.1 M $H_2SO_4$ at 20 mV $s^{-1}$. Voltammograms are normalized to (A) total electrode mass and (B) ECSA.

also in X-ray absorption near-edge spectra (XANES) data located in Figure S2 (Supporting Information). The annealed $Pt_{64}Ru_{36}$NTs demonstrate metallic Ru character similar to the Ru standard, which is in agreement with the X-ray diffraction data presented in Figure 4. There is a slight edge shift in the annealed sample compared to the Ru metal standard, likely from the formation of surface oxides. This is confirmed by the observation of oxides on the surfaces of the interior walls of the $Pt_{58}Ru_{42}$NTs in the HRTEM image in Figure 3f and such oxides are expected to be reduced to some degree during the methanol oxidation experiments.[56]

The substantial reduction in mass activity of the alloyed PtRuNTs is strongly influenced by changes in the catalyst structure that occur during the heat treatment at 750 °C, namely, reductions in ECSA and Pt utilization. Prior to heat treatment, the as-synthesized $PtRu(O_xH_y)$NTs have finely textured surfaces with considerably higher ECSAs than alloyed $Pt_{64}Ru_{36}$NTs due to a surface roughness not observed in the alloyed $Pt_{64}Ru_{36}$NTs. The SEM and TEM images in Figures 1a–d and 3a–d, respectively, reveal the fine nanoparticulate nature of the $PtRu(O_xH_y)$NT surfaces while the annealed PtRuNT surfaces (Figure 1e–h) are smoother from the grain coarsening and surface relaxation induced by the high-temperature treatment. In the alloyed $Pt_{64}Ru_{36}$NTs (Figure 9d), Pt has diffused within the 15–25 nm thick walls of the nanotubes during the heat treatment where it would not be accessible for methanol adsorption and dehydrogenation. However, in the as-synthesized, Pt-decorated nanotubes, catalytically active Pt would only be inaccessible when thick Pt layers or clusters formed during the synthesis of more-Pt-rich samples. The methanol oxidation currents were normalized by the ECSAs measured during CO stripping voltammetry in Figure 9B, and specific activities at 0.65 V are reported in Table 1. At 0.65 V vs RHE, the alloyed $Pt_{64}Ru_{36}$NTs with considerably lower surface area demonstrated specific activity (0.33 mA/$cm^2$) comparable to that of the as-synthesized nanotube sample with similar composition (0.39 mA/$cm^2$) and 1.5 times the specific activity of the commercial PtRu black (0.22 mA/$cm^2$). Of the highlighted nanotube catalysts in Figure 9, only the as-synthesized $Pt_{17}Ru_{83}(O_xH_y)$NT sample with significantly less Pt had a lower intrinsic activity than the commercial PtRu black (50% Pt). With a considerable reduction in Pt content from 64% Pt to 17% Pt in these $Pt_{17}Ru_{83}(O_xH_y)$NTs in Figure 9, the promotional effect of the underlying $Ru(O_xH_y)$ on Pt is more distinct, as the sample reaches a peak current for methanol oxidation at a potential 52 mV lower than the more-Pt-rich $Pt_{64}Ru_{36}(O_xH_y)$NTs.

The experimental nanotube catalysts discussed here represent a broad range of Pt composition; therefore, we also consider the catalysts' Pt content in the context of activity. Sample activity per unit of Pt mass and also sample activity normalized to Pt mass and sample ECSA, here referred to as Pt specific activity, are recorded at 0.65 V vs RHE and reported in Table 1. Considering the high activities of the as-synthesized nanotubes, it may be interesting to consider the potential for these dual-layer nanotubes following a third consecutive vapor deposition of a final interior layer of Pt. This resulting nanotube would be composed of three distinct layers, Pt–$Ru(O_xH_y)$–Pt, with active surfaces at both the exterior and the interior of the hollow nanotube promising further improvements in mass activity.

## 4. CONCLUSIONS

We have detailed the synthesis of monometallic, layered bimetallic, and alloyed bimetallic nanotubes by a novel method based on templated vapor deposition from metal acetylacetonate precursors. Prior to recovery from sacrificial anodic alumina templates, the nanotubes may be thermally annealed to induce a host of chemical and structural evolutions with significant implications on their catalytic activity. Hydrous Ru oxide was reduced to metal during heat treatment in a forming gas, yielding Pt–Ru alloys with composition-dependent crystal structures. Annealed PtRuNTs demonstrated nonuniform, nanoscale porosity as a result of observed grain size increases of approximately 3 times after 1 h at 750 °C.

Alloyed PtRuNTs demonstrated improved CO stripping kinetics compared to their as-synthesized $PtRu(O_xH_y)$NT counterparts as a result of the increased dispersion of Pt and Ru following thermal treatment. However, $PtRu(O_xH_y)$NTs had a higher Pt utilization and higher electrochemically active surface areas than alloyed PtRuNTs. Despite relatively poor CO stripping kinetics, the as-synthesized, Pt-decorated, hydrous ruthenium oxide nanotubes demonstrated higher mass activities than alloyed platinum–ruthenium nanotubes at 0.65 V vs RHE. With performance normalized to ECSA, $PtRu(O_xH_y)$NTs and alloyed $Pt_{64}Ru_{36}$NTs demonstrated 1.5 times the activity for methanol oxidation than PtRu black at 0.65 V vs RHE.


DOI: 10.1021/am508228b
ACS Appl. Mater. Interfaces 2015, 7, 10115–10124

The methods we demonstrate here are broadly applicable to the synthesis of high surface area, extended metal and oxide surfaces with tunable composition and microstructure. Though we demonstrate applications for electrooxidation of simple alcohols here, the materials palette made available via this approach is appropriate for a host of catalysis applications.

## ■ ASSOCIATED CONTENT

### Supporting Information

Additional figures containing structural characterizations (XRD, XANES, XPS). The Supporting Information is available free of charge on the ACS Publications website at DOI: 10.1021/am508228b.

## ■ AUTHOR INFORMATION

### Corresponding Author

*E-mail: apapandr@utk.edu.

### Notes

The authors declare no competing financial interest.

## ■ ACKNOWLEDGMENTS

This work is supported by the National Science Foundation through TN-SCORE (EPS-1004083). Microscopy was conducted as part of a user proposal at ORNL's Center for Nanophase Materials Sciences (CNMS), which is an Office of Science User Facility. A portion of this work (GMV-XPS) was supported by the U.S. Department of Energy (DOE), Basic Energy Sciences (BES), Materials Sciences and Engineering Division. Use of the National Synchrotron Light Source, Brookhaven National Laboratory, was supported by the U.S. Department of Energy, Office of Science, Office of Basic Energy Sciences, under Contract No. DE-AC02-98CH10886.

## ■ REFERENCES

(1) Van der Vliet, D. F.; Wang, C.; Tripkovic, D.; Strmcnik, D.; Zhang, X. F.; Debe, M. K.; Atanasoski, R. T.; Markovic, N. M.; Stamenkovic, V. R. Mesostructured Thin Films as Electrocatalysts with Tunable Composition and Surface Morphology. *Nat. Mater.* **2012**, *11*, 1051−1058.

(2) Debe, M. K. Nanostructured Thin Film Electrocatalysts for PEM Fuel Cells—A Tutorial on the Fundamental Characteristics and Practical Properties of NSTF Catalysts. *ECS Trans.* **2012**, *45*, 47−68.

(3) Ji, C.; Searson, P. C. Fabrication of Nanoporous Gold Nanowires. *Appl. Phys. Lett.* **2002**, *81*, 4437−4439.

(4) Sun, S.; Jaouen, F.; Dodelet, J.-P. Controlled Growth of Pt Nanowires on Carbon Nanospheres and Their Enhanced Performance as Electrocatalysts in PEM Fuel Cells. *Adv. Mater.* **2008**, *20*, 3900−3904.

(5) Chen, Z.; Waje, M.; Li, W.; Yan, Y. Supportless Pt and PtPd Nanotubes as Electrocatalysts for Oxygen-Reduction Reactions. *Angew. Chem., Int. Ed. Engl.* **2007**, *46*, 4060−4063.

(6) Garbarino, S.; Ponrouch, A.; Pronovost, S.; Gaudet, J.; Guay, D. Synthesis and Characterization of Preferentially Oriented (100) Pt Nanowires. *Electrochem. Commun.* **2009**, *11*, 1924−1927.

(7) Koenigsmann, C.; Scofield, M. E.; Liu, H.; Wong, S. S. Designing Enhanced One-Dimensional Electrocatalysts for the Oxygen Reduction Reaction: Probing Size-and Composition-Dependent Electrocatalytic Behavior in. *J. Phys. Chem. Lett.* **2012**, *3*, 3385−3398.

(8) Xia, Y.; Yang, P.; Sun, Y.; Wu, Y.; Mayers, B.; Gates, B.; Yin, Y.; Kim, F.; Yan, H. One-Dimensional Nanostructures: Synthesis, Characterization, and Applications. *Adv. Mater.* **2003**, *15*, 353−389.

(9) Subhramannia, M.; Pillai, V. K. Shape-Dependent Electrocatalytic Activity of Platinum Nanostructures. *J. Mater. Chem.* **2008**, *18*, 5858−5870.

(10) Cademartiri, L.; Ozin, G. A. Ultrathin Nanowires-A Materials Chemistry Perspective. *Adv. Mater.* **2009**, *21*, 1013−1020.

(11) Shao, Y.; Yin, G.; Gao, Y. Understanding and Approaches for the Durability Issues of Pt-Based Catalysts for PEM Fuel Cell. *J. Power Sources* **2007**, *171*, 558−566.

(12) Darling, R. M.; Meyers, J. P. Kinetic Model of Platinum Dissolution in PEMFCs. *J. Electrochem. Soc.* **2003**, *150*, A1523.

(13) Koenigsmann, C.; Wong, S. S. One-Dimensional Noble Metal Electrocatalysts: A Promising Structural Paradigm for Direct Methanol Fuel Cells. *Energy Environ. Sci.* **2011**, *4*, 1161−1176.

(14) Alia, S. M.; Yan, Y. S.; Pivovar, B. S. Galvanic Displacement as a Route to Highly Active and Durable Extended Surface Electrocatalysts. *Catal. Sci. Technol.* **2014**, *4*, 3589−3600.

(15) Sun, Y.; Xia, Y. Triangular Nanoplates of Silver: Synthesis, Characterization, and Use as Sacrificial Templates For Generating Triangular Nanorings of Gold. *Adv. Mater.* **2003**, *15*, 695−699.

(16) Koenigsmann, C.; Semple, D. B.; Sutter, E.; Tobierre, S. E.; Wong, S. S. Ambient Synthesis of High-Quality Ruthenium Nanowires and the Morphology-Dependent Electrocatalytic Performance of Platinum-Decorated Ruthenium Nanowires and Nanoparticles in the Methanol Oxidation Reaction. *ACS Appl. Mater. Interfaces* **2013**, *5*, 5518−5530.

(17) Leskelä, M.; Ritala, M. Atomic Layer Deposition Chemistry: Recent Developments and Future Challenges. *Angew. Chem.* **2003**, *42*, 5548−5554.

(18) Narayanan, R.; El-Sayed, M. A. Catalysis with Transition Metal Nanoparticles in Colloidal Solution: Nanoparticle Shape Dependence and Stability. *J. Phys. Chem. B* **2005**, *109*, 12663−12676.

(19) Borodko, Y.; Habas, S. E.; Koebel, M.; Yang, P.; Frei, H.; Somorjai, G. A. Probing the Interaction of Poly(vinylpyrrolidone) with Platinum Nanocrystals by UV-Raman and FTIR. *J. Phys. Chem. B* **2006**, *110*, 23052−23059.

(20) Yang, H.; Tang, Y.; Zou, S. Electrochemical Removal of Surfactants from Pt Nanocubes. *Electrochem. Commun.* **2014**, *38*, 134−137.

(21) Papandrew, A. B.; Wilson, D. L., III; M. Cantillo, N.; Hawks, S.; Atkinson, R. W., III; Goenaga, G. A.; Zawodzinski, T. A., Jr. Electrochemical Hydrogen Separation via Solid Acid Membranes. *J. Electrochem. Soc.* **2014**, *161*, F679−F685.

(22) Sivakumar, P.; Ishak, R.; Tricoli, V. Novel Pt−Ru Nanoparticles Formed by Vapour Deposition as Efficient Electrocatalyst for Methanol Oxidation Part I. Preparation and Physical Characterization. *Electrochim. Acta* **2005**, *50*, 3312−3319.

(23) Mercado-Zúñiga, C.; Vargas-García, J. R.; Hernández-Pérez, M. A.; Figueroa-Torres, M. Z.; Cervantes-Sodi, F.; Torres-Martínez, L. M. Synthesis of Highly Dispersed Platinum Particles on Carbon Nanotubes by an in Situ Vapor-Phase Method. *J. Alloys Compd.* **2014**, *615*, S538−S541.

(24) Bregoli, L. J. The Influence of Platinum Crystallite Size on the Electrochemical Reduction of Oxygen in Phosphoric Acid. *Electrochim. Acta* **1978**, *23*, 489−492.

(25) Nesselberger, M.; Ashton, S.; Meier, J. C.; Katsounaros, I.; Mayrhofer, K. J. J.; Arenz, M. The Particle Size Effect on the Oxygen Reduction Reaction Activity of Pt Catalysts: Influence of Electrolyte and Relation to Single Crystal Models. *J. Am. Chem. Soc.* **2011**, *133*, 17428−17433.

(26) Ohyama, J.; Sato, T.; Yamamoto, Y.; Arai, S. Satsuma, A. Size Specifically High Activity of Ru Nanoparticles for Hydrogen Oxidation Reaction in Alkaline Electrolyte. *J. Am. Chem. Soc.* **2013**, *135*, 8016−8021.

(27) Papandrew, A. B.; Atkinson, R. W., III; Goenaga, G. A.; Kocha, S. S.; Zack, J. W.; Pivovar, B. S.; Zawodzinski, T. A., Jr. Oxygen Reduction Activity of Vapor-Grown Platinum Nanotubes. *J. Electrochem. Soc.* **2013**, *160*, F848−F852.

(28) Wasmus, S.; Küver, A. Methanol Oxidation and Direct Methanol Fuel Cells: A Selective Review. *J. Electroanal. Chem.* **1999**, *461*, 14−31.

(29) Gilman, S. The Mechanism of Electrochemical Oxidation of Carbon Monoxide and Methanol on Platinum. II. The "Reactant-Pair"

Mechanism for Electrochemical Oxidation of Carbon Monoxide and Methanol. *J. Phys. Chem.* **1964**, *68*, 70−80.
(30) McCallum, C.; Pletcher, D. An Investigation of the Mechanism of the Oxidation of Carbon Monoxide Adsorbed Onto a Smooth Pt Electrode in Aqueous Acid. *J. Electroanal. Chem.* **1976**, *70*, 277−290.
(31) Love, B.; Lipkowski, J. Effect of Surface Crystallography on Electrocatalytic Oxidation of Carbon Monoxide on Platinum Electrodes. *ACS Symp. Ser.* **1988**, 484−496.
(32) Petukhov, A. V.; Akemann, W.; Friedrich, K. A.; Stimming, U. Kinetics of Electrooxidation of a CO Monolayer at the Platinum/Electrolyte Interface. *Surf. Sci.* **1998**, *402*−*404*, 182−186.
(33) Maillard, F.; Savinova, E. R.; Stimming, U. CO Monolayer Oxidation on Pt Nanoparticles: Further Insights Into the Particle Size Effects. *J. Electroanal. Chem.* **2007**, *599*, 221−232.
(34) Ticanelli, E.; Beery, J. G.; Paffett, M. T.; Gottesfeld, S. An Electrochemical, Ellipsometric, and Surface Science Investigation of the PtRu Bulk Alloy Surface. *J. Electroanal. Chem. Interfacial Electrochem.* **1989**, *258*, 61−77.
(35) Watanabe, M.; Motoo, S. Electrocatalysis by Ad-Atoms Part II. Enhancement of the Oxidation of Methanol On Platinum By Ruthenium Ad-Atoms. *Electroanal. Chem. Interfacial Electrochem.* **1975**, *60*, 267−273.
(36) Long, J. W.; Stroud, R. M.; Swider-Lyons, K. E.; Rolison, D. R. How To Make Electrocatalysts More Active for Direct Methanol Oxidation—Avoid PtRu Bimetallic Alloys! *J. Phys. Chem. B* **2000**, *104*, 9772−9776.
(37) Gasteiger, H. A.; Markovic, N.; Ross, P. N., Jr.; Cairns, E. J. Methanol Electrooxidation on Well-Characterized Pt-Ru Alloys. *J. Phys. Chem.* **1993**, *97*, 12020−12029.
(38) Gasteiger, H. A.; Markovic, N.; Ross, P. N., Jr.; Cairns, E. J. CO Electrooxidation on Well-Characterized Pt−Ru Alloys. *J. Phys. Chem.* **1994**, *98*, 617−625.
(39) Scott, F. J.; Mukerjee, S.; Ramaker, D. E. Contrast in Metal-Ligand Effects on $Pt_nM$ Electrocatalysts with M Equal Ru vs Mo and Sn As Exhibited by in Situ XANES and EXAFS Measurements in Methanol. *J. Phys. Chem. C* **2010**, *114*, 442−453.
(40) Guo, Y.-G.; Hu, J.-S.; Zhang, H.-M.; Liang, H.-P.; Wan, L.-J.; Bai, C.-L. Tin/Platinum Bimetallic Nanotube Array and Its Electrocatalytic Activity for Methanol Oxidation. *Adv. Mater.* **2005**, *17*, 746−750.
(41) Koenigsmann, C.; Sutter, E.; Adzic, R. R.; Wong, S. S. Size- and Composition-Dependent Enhancement of Electrocatalytic Oxygen Reduction Performance in Ultrathin Palladium−Gold ($Pd_{1-x}Au_x$) Nanowires. *J. Phys. Chem. C* **2012**, *116*, 15297−15306.
(42) Alia, S. M.; Jensen, K. O.; Pivovar, B. S.; Yan, Y. Platinum-Coated Palladium Nanotubes as Oxygen Reduction Reaction Electrocatalysts. *ACS Catal.* **2012**, *2*, 858−863.
(43) Alia, S. M.; Pivovar, B. S.; Yan, Y. Platinum-Coated Copper Nanowires with High Activity for Hydrogen Oxidation Reaction in Base. *J. Am. Chem. Soc.* **2013**, *135*, 13473−13478.
(44) Alia, S. M.; Pylypenko, S.; Neyerlin, K. C.; Cullen, D. A.; Kocha, S. S.; Pivovar, B. S. Platinum-Coated Cobalt Nanowires as Oxygen Reduction Reaction Electrocatalysts. *ACS Catal.* **2014**, *4*, 2680−2686.
(45) Alia, S. M.; Larsen, B. A.; Pylypenko, S.; Cullen, D. A.; Diercks, D. R.; Neyerlin, K. C.; Kocha, S. S.; Pivovar, B. S. Platinum-Coated Nickel Nanowires as Oxygen-Reducing Electrocatalysts. *ACS Catal.* **2014**, *4*, 1114−1119.
(46) Shao, M.; Odell, J. H.; Choi, S.-I.; Xia, Y. Electrochemical Surface Area Measurements of Platinum- and Palladium-Based Nanoparticles. *Electrochem. Commun.* **2013**, *31*, 46−48.
(47) Rolison, D. R.; Hagans, P. L.; Swider, K. E.; Long, J. W. Role of Hydrous Ruthenium Oxide in Pt−Ru Direct Methanol Fuel Cell Anode Electrocatalysts: The Importance of Mixed Electron/Proton Conductivity. *Langmuir* **1999**, *15*, 774−779.
(48) Zheng, J. P.; Cygan, P. J.; Jow, T. R. Hydrous Ruthenium Oxide as an Electrode Material for Electrochemical Capacitors. *J. Electrochem. Soc.* **1995**, *142*, 2699−2703.
(49) Hamel, C.; Garbarino, S.; Irissou, E.; Bichat, M.-P.; Guay, D. Structural and Electrochemical Properties of Nanocrystalline PtRu Alloys Prepared by Crossed-Beam Pulsed Laser Deposition. *J. Phys. Chem. C* **2010**, *114*, 18931−18939.
(50) Ma, J.-H.; Feng, Y.-Y.; Yu, J.; Zhao, D.; Wang, A.-J.; Xu, B.-Q. Promotion by Hydrous Ruthenium Oxide of Platinum for Methanol Electro-Oxidation. *J. Catal.* **2010**, *275*, 34−44.
(51) Friedrich, K. A.; Henglein, F.; Stimming, U.; Unkauf, W. Size Dependence of the CO Monolayer Oxidation on Nanosized Pt Particles Supported on Gold. *Electrochim. Acta* **2000**, *45*, 3283−3293.
(52) Arenz, M.; Mayrhofer, K. J. J.; Stamenkovic, V.; Blizanac, B. B.; Tomoyuki, T.; Ross, P. N.; Markovic, N. M. The Effect of the Particle Size on the Kinetics of CO Electrooxidation on High Surface Area Pt Catalysts. *J. Am. Chem. Soc.* **2005**, *127*, 6819−6829.
(53) Godoi, D. R.; Perez, J.; Villullas, H. M. Effects of Alloyed and Oxide Phases on Methanol Oxidation of Pt−Ru/C Nanocatalysts of the Same Particle Size. *J. Phys. Chem. C* **2009**, *113*, 8518−8525.
(54) Park, Y.-K.; Kim, T.-H.; Park, S. Designer Composite Materials Fabricated From Platinum and Ruthenium Nanoparticles. *J. Mater. Chem.* **2010**, *20*, 3637−3641.
(55) McKeown, D. A.; Hagans, P. L.; Carette, L. P. L.; Russell, A. E.; Swider, K. E.; Rolison, D. R. Structure of Hydrous Ruthenium Oxides. *Implications for Charge Storage* **1999**, *103*, 4825−4832.
(56) Stoupin, S.; Chung, E. H.; Chattopadhyay, S.; Segre, C. U.; Smotkin, E. S. Pt and Ru X-ray Absorption Spectroscopy of PtRu Anode Catalysts in Operating Direct Methanol Fuel Cells. *J. Phys. Chem. B* **2006**, *110*, 9932−9938.


DOI: 10.1021/am508228b
*ACS Appl. Mater. Interfaces* 2015, 7, 10115−10124